



Unraveling soft breakdown in solid-state electrolytes

Haoqi Ren^a, Yu Zhong^c, Xiaoting Lin^a, Jiamin Fu^a, Jing Luo^a, Yang Hu^a, Yipeng Sun^a, Heng-Yong Nie^{d,e}, Han Su^{a,c}, Weihan Li^a, Feipeng Zhao^a, Yu Liu^a, Jung Tae Kim^a, Mingrui Yang^a, Changhong Wang^{a,b,*}, Xueliang Sun^{a,b,*}

^a Department of Mechanical and Materials Engineering, University of Western Ontario, 1151 Richmond St, London, Ontario N6A 3K7, Canada

^b Eastern Institute for Advanced Study, Eastern Institute of Technology, Ningbo, Zhejiang 315200, China

^c State Key Laboratory of Silicon Materials, Key Laboratory of Advanced Materials and Applications for Batteries of Zhejiang Province, School of Materials Science and Engineering, Zhejiang University, Hangzhou 310027, China

^d Surface Science Western, University of Western Ontario, 999 Collip Circle, London, Ontario N6G 0J3, Canada

^e Department of Physics and Astronomy, University of Western Ontario, 1151 Richmond St, London, Ontario N6A 3K7, Canada

ARTICLE INFO

Keywords:
All solid-state batteries
Soft breakdown
Asymmetric cells
Lithium Dendrites
Solid state interphase

ABSTRACT

All-solid-state lithium metal batteries (ASSLMBs) with solid-state electrolytes (SSEs) are regarded as next-generation energy storage technology due to their superior safety and exceptional energy density. However, soft breakdown—a prevalent failure mechanism in ASSLMBs—has hindered their development. In this study, we introduce Li/SSE/current collector (CC) asymmetric cells as a novel evaluation method to assess the susceptibility of various SSEs to soft breakdown. Our findings reveal that metal-contained SSEs (e.g., LGPS) exhibit a stronger resistance to soft breakdown compared to metal-free SSEs (e.g., LPSC) through phase characterization including ToF-SIMS and XPS. This enhanced stability is attributed to the formation of a metal-containing solid electrolyte interphase (SEI) at the interface. Moreover, the impact of practical cell configuration including current density, stack pressure, cutoff voltage on the occurrence of soft breakdown was also discussed. The insights gained from this work deepen the understanding of the soft breakdown phenomenon in SSEs and provide valuable guidance for the design of advanced solid-state electrolytes.

1. Introduction

Lithium metal stands out as an optimal candidate for an anode material due to its high theoretical specific capacity of 3860 mAh.g^{-1} and exceptionally low electrochemical potential of -3.040 V vs. the standard hydrogen electrode.^[1,2] These attributes hold the promise of significantly augmenting the energy density of lithium-ion batteries (LIBs).^[3,4] However, the integration of Li metal anodes into LIBs has been hindered by challenges associated with non-uniform and irreversible lithium deposition. This issue leads to lithium dendrite growth, significant volume change, and irreversible interfacial reactions, ultimately compromising battery lifespan and posing safety hazards.^[5,6] To address these challenges, solid-state electrolytes (SSEs) have emerged as a promising solution due to their high elastic modulus.^[7–9] Moreover, substituting flammable liquid organic electrolytes with SSEs can alleviate the safety concerns inherent to LIBs.^[10–14] For these merits,

substantial research efforts have been devoted to developing all-solid-state lithium metal batteries (ASSLMBs) in recent years.

In the realm of ASSLMBs, soft breakdown, also referred to as "soft shorts", "micro short circuits", "dynamic short circuits", and "internal short circuits", has become a significant cell failure mechanism.^[10, 15–22] Unlike hard breakdown, which results in permanent battery failure, soft breakdown does not immediately short the battery but arises during battery operation and is difficult to identify. Compared to liquid counterparts, ASSLMBs are more prone to experiencing soft breakdown due to the high electronic conductivity of solid-state electrolytes (SSEs), insufficient solid-solid interface contact, and uneven localized electric fields. However, what kinds of SSEs have strong capability to inhibit the occurrence of soft breakdowns have not been explored yet.

In this study, using a Li/SSE/current collector (CC) asymmetric cell configuration, we demonstrate that LGPS exhibits superior resistance to soft breakdown but lower Coulombic efficiency of Li^+ ions compared to

* Correspondence to: Department of Mechanical and Materials Engineering, University of Western Ontario, London, Ontario N6A 5B9, Canada; Eastern Institute for Advanced Study, Eastern Institute of Technology, Ningbo, Zhejiang 315200, China.

E-mail addresses: cwang@eitech.edu.cn (C. Wang), xsun9@uwo.ca (X. Sun).

LPSC and LPS. This finding suggests that metal-contained solid-state electrolytes can effectively suppress the occurrence of soft breakdown but face the issue of low Coulombic efficiency. Further interface characterization using TOF-SIMS and Raman spectroscopy reveals that the formation of a Li-Ge alloy at the interface minimizes lithium dendrite growth, thereby preventing soft breakdown. These results indicate that the chemical composition of SSEs plays a critical role in the SEI, which in turns influences cycling stability of ASSLMBs. We believe this work advances the understanding of the soft breakdown phenomenon in ASSLBs and offers new insights into solid electrolyte design for achieving long-term, stable cycling in ASSLMBs.

2. Results and discussion

In this study, we employed Li/SSE/current collector (CC) asymmetric cells to evaluate the susceptibility of various solid-state electrolytes (SSEs) to soft breakdown. Compared to conventional Li/SSE/Li symmetric cells, the Li/SSE/CC asymmetric configuration offers several distinct advantages in assessing SSE resistance to soft breakdown. First, Li/SSE/CC asymmetric cells enable rapid detection of soft breakdown, a capability lacking in traditional symmetric cells. Second, the Coulombic efficiency (CE) can be measured in each cycle for Li/SSE/CC cells, providing real-time insight into the cell's health. In contrast, Li/SSE/Li symmetric cells consistently exhibit 100 % CE, masking early signs of degradation. A sudden drop in CE in asymmetric cells serves as a clear indicator of soft breakdown. Third, the challenge of obtaining a clean surface for solid electrolyte interphase (SEI) analysis—due to the sticky nature of lithium metal in symmetric cells—is mitigated in asymmetric cells, simplifying interfacial characterization. Lastly, symmetric cells cannot evaluate the impact of applied voltage since both electrodes are identical. In contrast, the cut-off voltage in Li/SSE/CC asymmetric cells can be customized, allowing the study of voltage effects on battery performance. However, it is important to note that the interfacial properties between the current collector and SSE significantly influence lithium plating and stripping behavior. Therefore, rational interface engineering—focusing on solid-solid contact and physicochemical compatibility—is crucial when utilizing Li/SSE/CC asymmetric cells for interfacial evaluation.

To prove the effectiveness of Li/SSE/CC asymmetric cells in assessing soft breakdown, Li/Li₆PS₅Cl (LPSC)/CC asymmetric cells and Li/LPSC/

Li symmetric cells are constructed and cycled with an areal capacity of 0.1 mAh·cm⁻² and a current density of 0.1 mA·cm⁻² (Figs. 2a and 2b). The symmetric cell can be cycled for 600 hours without an obvious voltage drop, while the asymmetric cell shows a sudden voltage drop in the third cycle, which indicates the occurrence of soft breakdown, as highlighted in Fig. 2c. The 4th and 5th cycles present normal charge behaviors, indicating the soft breakdown is recoverable. The impedance of the asymmetric cell during cycling is also found in Figure S1. As shown in Figure S1, the impedance of the cell before cycling was around 154 Ω. Then after 5 cycles, it increased to 207 Ω because of the interfacial reaction between electrodes and LPSC, while the slope of low-frequency area decreased indicating the increase of electronic conductivity.[23] After 20 cycles, the impedance dropped to 32 Ω and the electronic conductive behavior served as the major charge transfer pathway at this time. It is in accordance with the soft short behavior of Li-asymmetric cells in Fig. 2a. To confirm if the soft breakdown is ubiquitous, we further test both symmetric cells and asymmetric cells using liquid electrolytes (Figure S2). The current density of 0.5, 1, 2, and 3 mA·cm⁻² is set in Li-Li symmetric cells, Li-Cu asymmetric cells, and Li-steel asymmetric cells (shown in Figure S2). It can be found that Li-Li symmetric cells can stably cycle for hundreds of hours with no pronounced change in polarization voltage, while Li-Cu and Li-stainless steel (SS) asymmetric cells can only operate for tens of hours before the appearance of voltage fluctuation, which indicates the occurrence of soft breakdown.

It should be noted that the physical and chemical states of current collectors have a significant influence on the occurrence of soft breakdown. Therefore, engineering the surface of the current collector is pivotal for extending the lifespan of Li-Cu asymmetric cells. To confirm the origin of soft short, a Li/LPSC/Au@Cu is tested under the capacity of 0.1 mAh·cm⁻² at a low current density of 0.1 mA·cm⁻² as well. The results in Fig. 2d show that the soft breakdown occurs at the 20th cycle, which is much later compared to using stainless steel (SS) electrodes. This delay can be attributed to the efficient diffusion of lithium in gold, which reduces the formation of micro-dendrites on the electrode surface.[24,25]. Li symmetric cell cycles stably for over 500 hours with only a slight increase in resistance. Therefore, Li-CC asymmetric cells can effectively detect the soft breakdown phenomenon as long as the surface of current collectors is rationally designed, while symmetric cells may exhibit misleading stability.

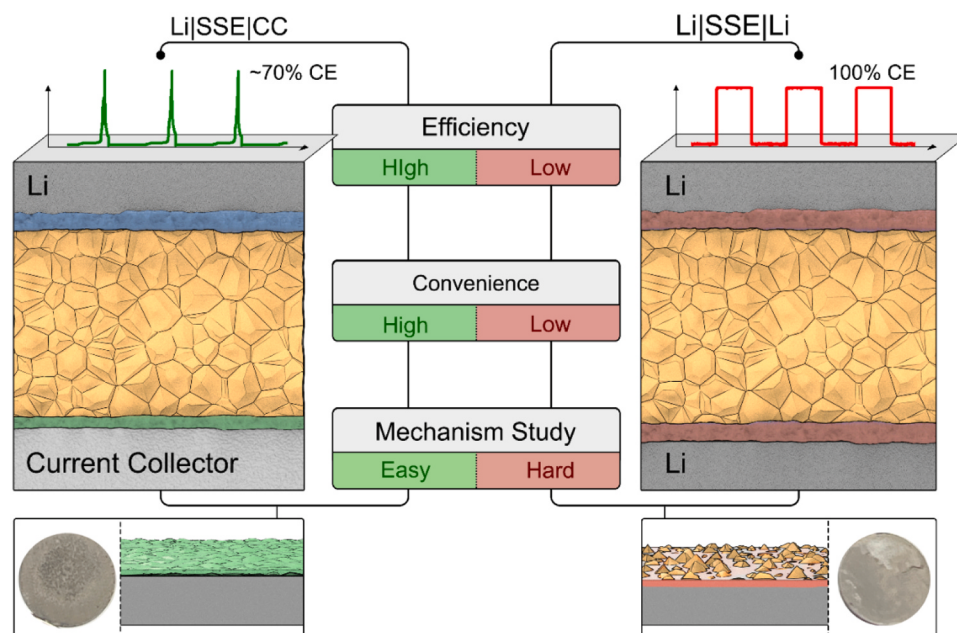


Fig. 1. Functionality Comparison of Li-Li symmetric cells and Li-CC asymmetric cells in soft breakdown evaluation.

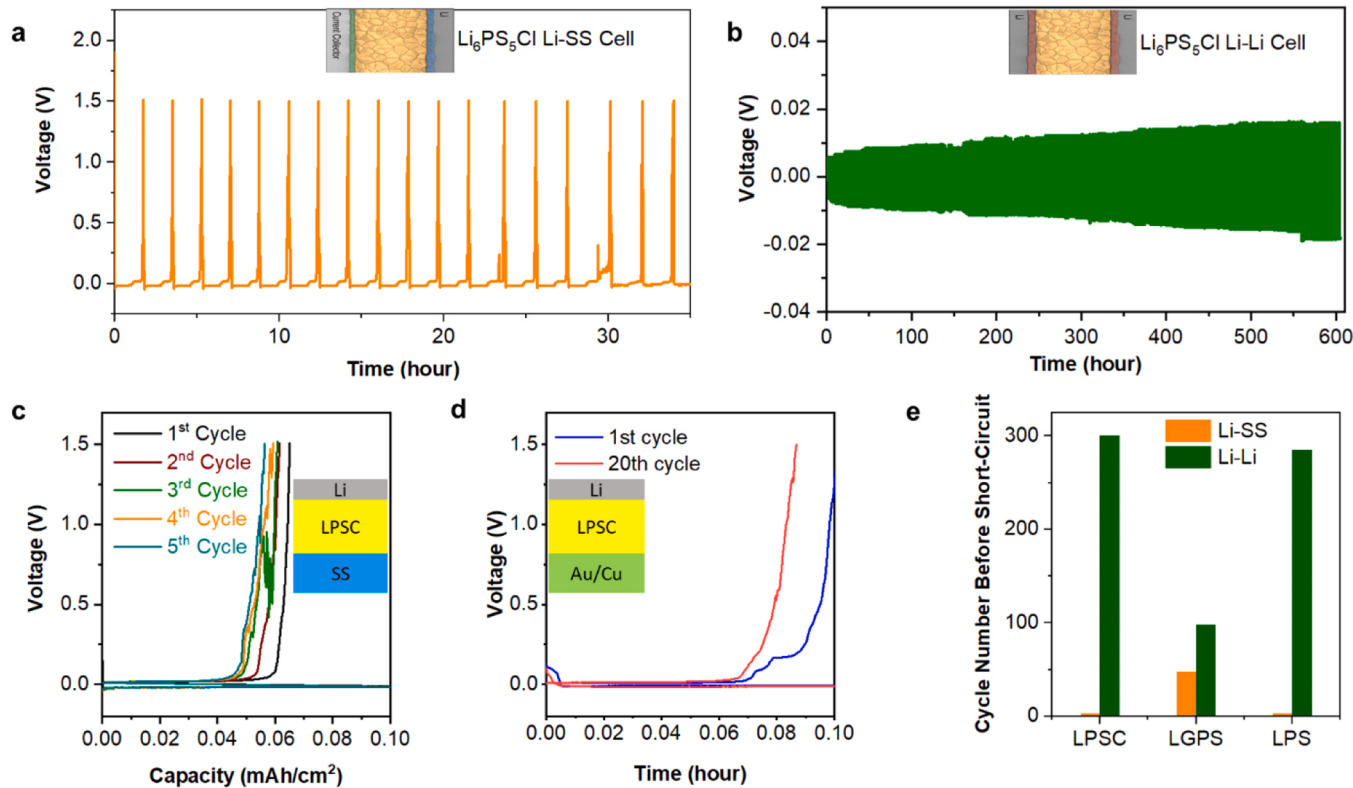


Fig. 2. Comparison between Li-CC asymmetric cells and Li-Li symmetric cells. (a) Cycling performance of Li/LPSC/steel asymmetric cells under the condition of $0.1 \text{ mA}\cdot\text{cm}^{-2}$ and $0.1 \text{ mAh}\cdot\text{cm}^{-2}$. (b) Cycling performance of Li/LPSC/Li symmetric cells under the condition of $0.1 \text{ mA}\cdot\text{cm}^{-2}$ and $0.1 \text{ mAh}\cdot\text{cm}^{-2}$. (c) Soft breakdown in the Li/LPSC/SS asymmetric cells from Fig. 2a. (d) Soft breakdown in the Li/LPSC/Au@Cu asymmetric cells. (e) Comparison of the occurrence of short-circuit in different sulfide-based SSEs in Li/SSE/CC and Li/SSE/Li cells.

Different SSEs exhibit varying abilities to prevent soft breakdown phenomena. To verify this, Li/Li₁₀GeP₂S₁₂(LGPS)/CC and Li/LGPS/Li cells are fabricated and analyzed. As shown in Figure S3a-S3b, Li/LGPS/Li symmetric cells can be stably cycled for 180 hours, albeit with a continuous increase in overpotential, which is due to the unstoppable interfacial reactions between Li and LGPS. The voltage drops after 180 hours, indicating the onset of soft breakdown. In contrast, the Li/LGPS/CC asymmetric cell shows a soft breakdown after 80 hours. The voltage fluctuation can be observed in the 40th cycle (Figure S3c-S3d). This comparison further demonstrates that the Li/SSE/Li symmetric cell overestimates Li/SSE interfacial stability because of its incapability to detect soft breakdown phenomena. Notably, the nucleation overpotential of Li on the current collector decreases from 83.7 mV to 59.8 mV (Figure S3e), suggesting changes in plating behavior during cycling.^[26] Compared with Li/LPSC/CC and Li/LPS/CC results (Figure S4), Li/LGPS/CC presents a better ability to prevent soft breakdown. The delayed occurrence of soft breakdown is attributed to the formation of a lithophilic Li-Ge layer, regulating lithium deposition and reducing dendrite growth. Fig. 2f highlights the varying abilities of sulfide SSEs to resist soft breakdown, with LPSC and LPS exhibiting higher susceptibility compared to LGPS. These comparative analyses suggest that Li/SSE/CC asymmetric cells provide a more direct assessment of an SSE's resistance to soft breakdown.

The soft breakdown will also be partially reflected by the change in Coulombic efficiency. The calculation of CE can be expressed as:

$$\text{CE}_{\text{Li}} = \frac{\text{C}_{\text{stripping}}}{\text{C}_{\text{plating}}} * 100\% \quad (1)$$

where CE_{Li} is the Coulombic efficiency of Li, $\text{C}_{\text{stripping}}$ and $\text{C}_{\text{plating}}$ is the stripping capacity and plating capacity, respectively. CE_{Li} is a significant parameter of ASSLMBs as it has a strong correlation with cycling stability.^[27,28] Thus, it is valuable that Li/SSE/CC asymmetric cells

can independently assess the CE and cycle life of different SSEs without the interference of anodic loss in full batteries. The CE of various sulfide SSEs is shown in Figs. 3a-3c. The CE of Li/LPSC/CC in the initial cycle is 65.1 %, decreasing gradually to 56.3 % by five cycles. The initial RE aligns with that of liquid electrolytes, primarily influenced by the physiochemical properties of current collectors.^[29] The initial five cycles do not show an abrupt change in RE, which is labeled as "a stable state" (green area). A sudden change of RE to 64.6 % occurs in the sixth cycle, implying the occurrence of soft breakdown. After the initial soft breakdown, the plating and stripping behaviors appear normal, suggesting soft breakdown is recoverable in this stage (marked as yellow area). Subsequently, CE sharply rises to 142.9 % in the fifteenth cycle, signifying increased severity of soft breakdown. Thereafter, the batteries frequently experience soft breakdowns, resulting in erratic CE jumps and voltage fluctuations (orange area). The CE change tendency of LPS is similar to that of LPSC (Fig. 3b) because they have similar SEI composition.^[30,31] In contrast, LGPS shows a much different behavior in CE compared with LPSC and LPS. The initial RE of Li/LGPS/SS is only 1.39 % (Fig. 3d), significantly lower than that of LPSC and LPS, suggesting more severe reactivity between LGPS and Li than between LPSC or LPS and Li. The first CE jump occurs in the 55th cycle, with abnormal charge-discharge behavior occurring after 150 cycles. This difference is attributed to the formation of a mixed electron/ion conductive interphase consisting of Li-Ge alloys, Li₃P, and Li₂S.^[32] The presence of Li-Ge alloy aids in regulating Li electrodeposition by alloying, thus inhibiting Li dendrite formation.^[9,33] Therefore, Li/LGPS/SS shows a longer "stable stage" and "recoverable stage" than Li/LPSC/SS and Li/LPS/CC counterparts.

Based on the above analyses, the dynamic process of soft breakdown is schematically illustrated in Fig. 3d. Initially, nano-/micro dendrites grow during the "stable stage", eventually leading to the first soft shorts. At this point, electron transport-induced leakage current causes voltage

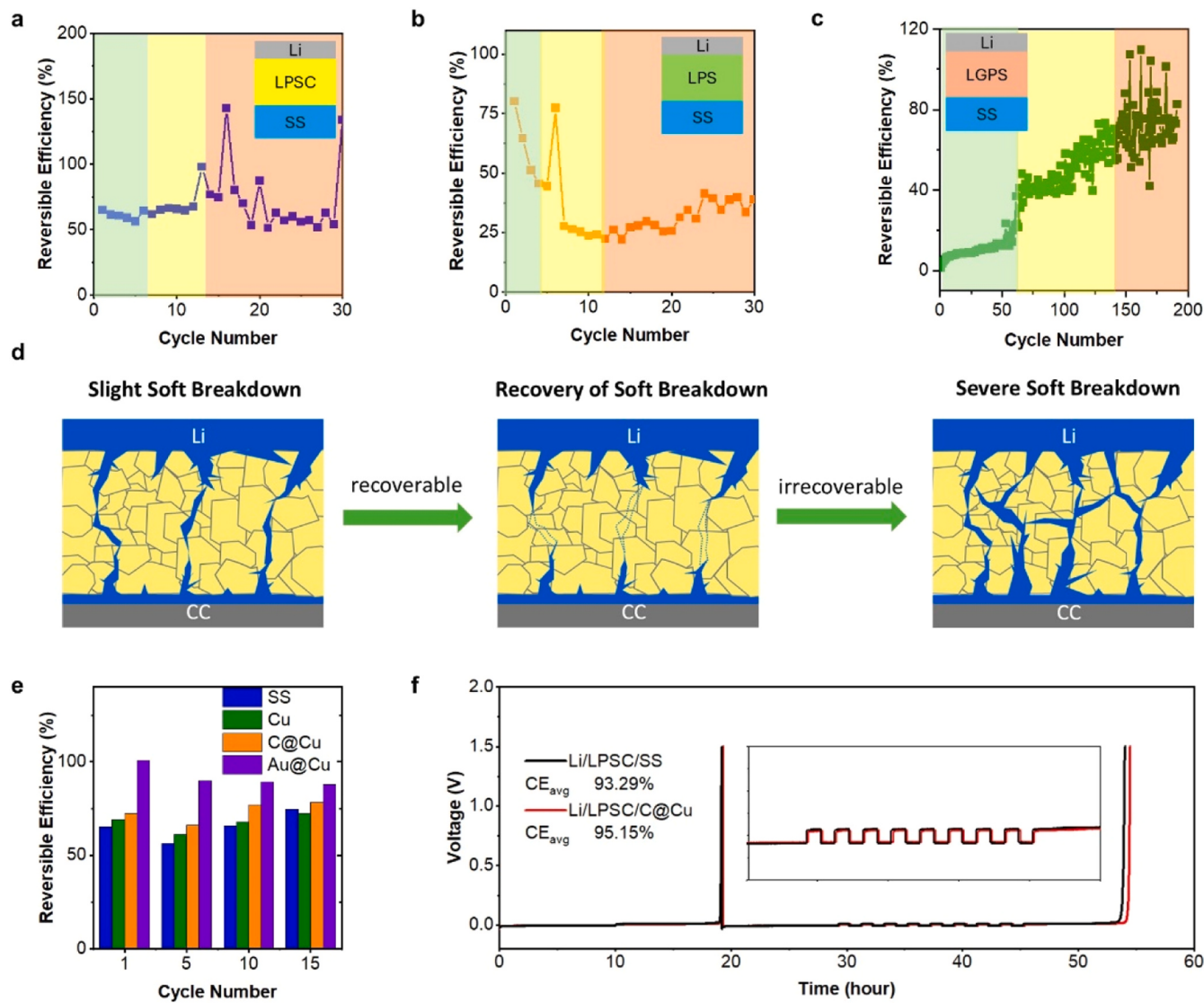


Fig. 3. Coulombic efficiency of different solid electrolytes using asymmetric cells. (a) CE of Li/LPSC/SS asymmetric cells under the conditions of $0.1 \text{ mA}/\text{cm}^2$ and $0.1 \text{ mAh}/\text{cm}^2$. (Green area: stable stage; Yellow area: recoverable stage with slight soft breakdown; Orange area: irrecoverable stage with severe soft breakdown) (b) CE of Li/LPS/SS asymmetric cells under the condition of $0.1 \text{ mA}/\text{cm}^2$ and $0.1 \text{ mAh}/\text{cm}^2$. (c) CE of Li/LGPS/SS asymmetric cells under the condition of $0.1 \text{ mA}/\text{cm}^2$ and $0.1 \text{ mAh}/\text{cm}^2$. (d) Scheme of soft breakdown evolution (e) Comparison of Coulombic efficiency of LPSC on different current collectors (f) Average CE of LPS and LPSC under the condition of $0.1 \text{ mA}/\text{cm}^2$ and $0.1 \text{ mAh}/\text{cm}^2$.

fluctuations. To compensate for the voltage drop, an overcharge phenomenon occurs, resulting in a jump in CE. However, the soft breakdown is relatively minor and can still be mitigated by the interfacial reaction between solid electrolytes and dendrites. As the connecting parts of the micro-dendrites are consumed, the batteries return to normal charge-discharge behavior in the “recoverable stage”. [34,35] With a sufficient number of cycles, accumulated micro-dendrites interconnect, leading to severe soft breakdown. This soft short cannot be fully rectified, and the voltage profile exhibits fluctuations in each cycle until a complete hard short occurs.

The CE of LPSC on different current collectors is compared in Fig. 3e. The initial RE of LPSC on C@Cu and Au@Cu is 72.28 % and 100.76 %, respectively, which is apparently higher than the initial RE of LPSC on SS and Cu. It manifests that the substrate can have a significant influence on the plating and stripping behavior of Li. Notably, the initial CE on Au@Cu was over 100 %, which can be attributed to the Li-Au alloying reaction. [36] The alloying reaction and fast diffusion kinetics of Li could effectively regulate the plating behavior and reduce the dendrite growth in Au@Cu. [25] In the following cycles, the Au@Cu anode could exhibit

a stable CE around 88 %, while the RE of C@Cu and SS went down first and exhibited sudden jump due to the potential soft breakdown. Therefore, surface engineering could be pivotal for improving the accuracy of CE assessment.

Apart from RE, we further examine the average CE of different SSE-based Li/CC asymmetric cells using a method described in previous studies. [37–39] In this method, a Li reservoir is deposited onto the current collector (Q_T), followed by cycling a fixed capacity of Li (Q_C) for a certain number of cycles (n). Finally, the Li remaining in the reservoir is completely stripped to a higher cut-off voltage (Q_S). The average CE can be calculated by the formula:

$$\text{CE}_{\text{avg}} = (nQ_C + Q_S)/(nQ_C + Q_T) * 100\% \quad (2)$$

The average CE of LPSC is shown in Fig. 3f. For Li/LPSC/C@Cu and Li/LPSC/SS, the average CE is 95.15 % and 93.29 %, respectively. This suggests that the average CE value remains consistent when different current collectors are used, indicating that this result is more accurate than RE because it eliminates the influence of current collectors. However, this method also has limitations. For instance, the average CE of Li/

LPS/C@Cu and Li/LPS/SS is 96.70 and 103.09 % (Figure. S5a), respectively. An average CE exceeding 100 % indicates the occurrence of soft breakdown during testing. In addition, this method cannot determine the average CE of some SSEs, such as LGPS (Figure. S5b), because LGPS shows severe interfacial reactions with Li, which consumes abundant Li, resulting in insufficient active Li available for the subsequent stripping process.

Besides the common sulfide SSEs, the cycling stability of nitride and halide SSEs was also examined (Figure. S6). The cell using Li_3N was tested with a cut-off voltage at 0.5 V, which is caused by the intrinsic electrochemical window of Li_3N is 0–0.6 V.[40,41] It is observed that the soft breakdown of Li_3N occurs in the first cycle due to its high electronic conductivity ($\sigma_e=8.8\times 10^{-7} \text{ S}\cdot\text{cm}^{-1}$) and large porosity (71.1 %). Moreover, the CE continues to decrease, possibly due to poor contact between lithium nitrides and current collectors. Furthermore, like LGPS, Li_3YCl_6 exhibits a similar behavior driven by interfacial reactions, with an initial CE as low as 20 % and more severe polarization. These results indicate the significant instability of lithium metal anode against these SSEs. In contrast, the CE of Li/SSE/Li symmetric cells always remain at 100 %, giving no hints on the soft breakdown. Therefore, these experimental analyses demonstrated that Li/SSE/CC asymmetric cells are a simple but straightforward method to diagnose the soft breakdown phenomenon and determine the RE and CE in solid-state batteries.

The Li/SSE/CC asymmetrical cells can provide a clean SSE/CC interface by simply peeling off the CC and enable us to explore the reason that soft breakdown behavior varies in LPSC and LGPS. The optical images of the raw surface of the LPSC before cycling and interface in Li-Li symmetric cells and Li-CC asymmetric cells are shown in Fig. 4a. The initial surface of LPSC pellets is smooth, while the surface of the pellet in Li-Li after the removal of Li becomes rough and some parts are fully removed since the Li metal is sticky.[42] In contrast, the interface of CC-LPSC is almost flat as the raw pellets. Moreover, the tiny black dots on the pellets would indicate the interfacial reaction between Li and LPSC. The SEM images in Figs. 4b and 4c show that the surface of the amount of crack increases after cycling, and charging-discharging products would occur in the form of small particles.

In order to compare the interface chemistry of the Li-LPSC and CC-LPSC, we used time-of-flight secondary ion mass spectrometry (ToF-SIMS) to depth profile the LPSC side with the Li and CC layer removed from the Li/SSE/Li and Li/SSE/CC cells, respectively.[43] ToF-SIMS is surface sensitive technique measuring the (secondary) ions generated from the outermost 1–3 nm of a surface upon bombardment of a primary ion beam, which can also be used to depth profile when using a sputter ion beam to remove controllable amounts of substance.[44] Shown in Figs. 4d–4f are ToF-SIMS results of depth profiles of negative ions P^- , Li^- , $^{34}\text{S}^-$, and PS_3^- , for the raw surface of LPSC, the interface of Li-LPSC and the interface of CC-LPSC, respectively. The reason to use $^{34}\text{S}^-$, rather

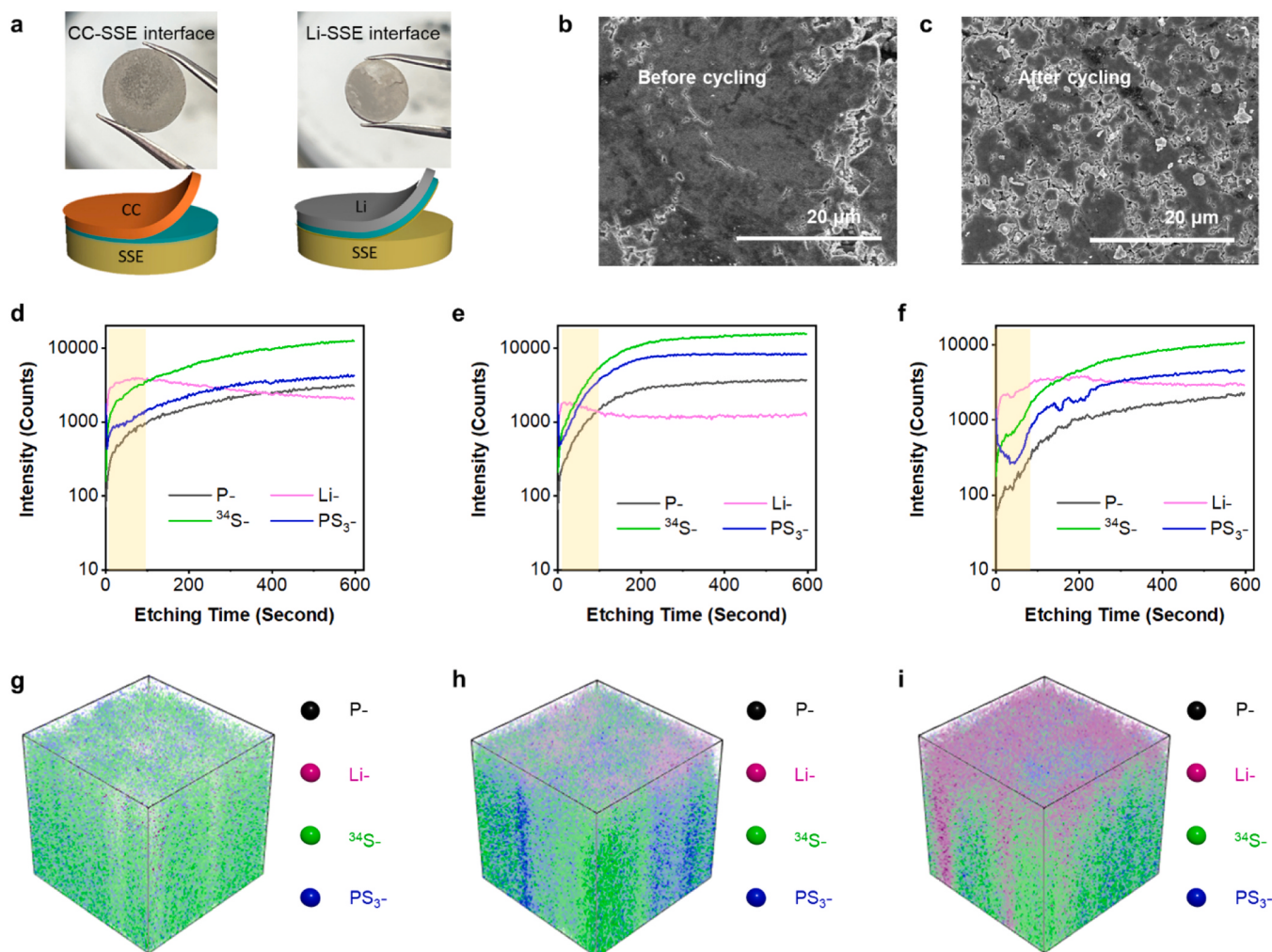


Fig. 4. Characterizations of the Li/SSE and CC/SSE interfaces. (a) Optical images from the top and schematic of the surface of Steel/LPSC (left) and Li/LPSC (right). (b) and (c) SEM images of the raw surface of LPSC and Steel/LPSC, respectively. (d) ToF-SIMS depth profile of the raw surface of LPSC. (e) ToF-SIMS depth profile of interface of Steel-LPSC. (f) ToF-SIMS depth profile of interface of Li-LPSC. (g)-(i) Corresponding 3D reconstruction (lateral dimensions: 128 μm × 128 μm) of element distribution of (d)-(f), respectively.

than $^{32}\text{S}^-$ the main sulfur isotopes, to represent sulfur is because the latter was too strong and saturated the detector. The depth profiles of P^- , Li^- , and $^{34}\text{S}^-$ are more or less similar to each other. However, the PS_3^- depth profiles reveal the difference among the three samples. The PS_3^- intensity is the lowest at the Li-LPSC interface (Fig. 4e) and monotonically increases towards the bulk, which behaves similarly to that of the raw pellet interface (Fig. 4d). Assuming the interior of LPSC pellets would not involve the electrochemistry reactions, it can be found only bulk LPSC remained after peeling off the lithium, and the SEI phase would be fully removed. By contrast, the PS_3^- intensity of CC-LPSC is observed to decrease up to a sputtering time of ~ 50 s, after which it increases (Fig. 4f) like those of the other two samples (Figs. 4d-4e). The layer defined by the valley of the PS_3^- depth profile, which is around 30 nm according to the estimated sputter rate of 0.3 nm/s, can be identified as the SEI phase. This is in agreement with the assumption that the SEI of LPSC is a LiCl-rich phase, which indicates that the concentrations of other anions are relatively lower.^[45,46] To validate our finding on assigning the PS_3^- valley to the SEI, its depth profile is compared with that of LiCl_2^- . As shown in Figure S7, the PS_3^- valley indeed corresponds to the LiCl_2^- peak. Therefore, our ToF-SIMS results verified that the SEI has increased and decreased amounts of LiCl_2^- and PS_3^- , respectively.

In the depth profile of an ion, each intensity is the sum of its intensity over the pixels (128×128) rostered at each sputter time (depth). 3D

reconstruction of an ion depth profile resolves its intensities (visualized by false color scales) over each pixel at each depth. The 3D reconstruction of the surface of raw LPSC pellets shows an even distribution of all ions (Fig. 4g), while the interface of Li-LPSC shows a similar distribution as raw LPSC with slight amount of Li concentrated on the surface (Fig. 4h). On the other hand, a large amount of Li concentrates on the top interface of CC-LPSC and some part of Li penetrates the LPSC, indicating the presence of dead lithium or lithium filaments (Fig. 4i). The comparison of uncycled and cycled LGPS is given in Fig. 5. It can be observed that severe destruction occurred in the Li-Li symmetric cell due to the stronger reaction activity between Li and LGPS (Fig. 5a). The SEM images for the interface before (Fig. 5b) and after (Fig. 5c) the cycling revealed a smoother interface upon reaction, attributable to the formation of Li-Ge alloy. According to the ToF-SIMS depth profiles in Figs. 5d-5f, along with their distribution in 3D in Figs. 5g-5i for pristine LGPS, Li-LGPS and Steel-LGPS, it can be confirmed that the S species (represented by $^{34}\text{S}^-$) remains relatively constant from the surface to the bulk in both raw pellets and pellets from symmetric cells. However, a clear depletion of S and other species, except for Li, is observed beneath the SEI surface from the pellets of asymmetric cells. It indicates the formation of Li-Ge alloy and thus an uneven distribution of the decomposition products. The formation of such a lithophilic layer helps reduce the occurrence of soft breakdown during cycling. Therefore, dendrite growth would occur more easily in the cell using non-metal-

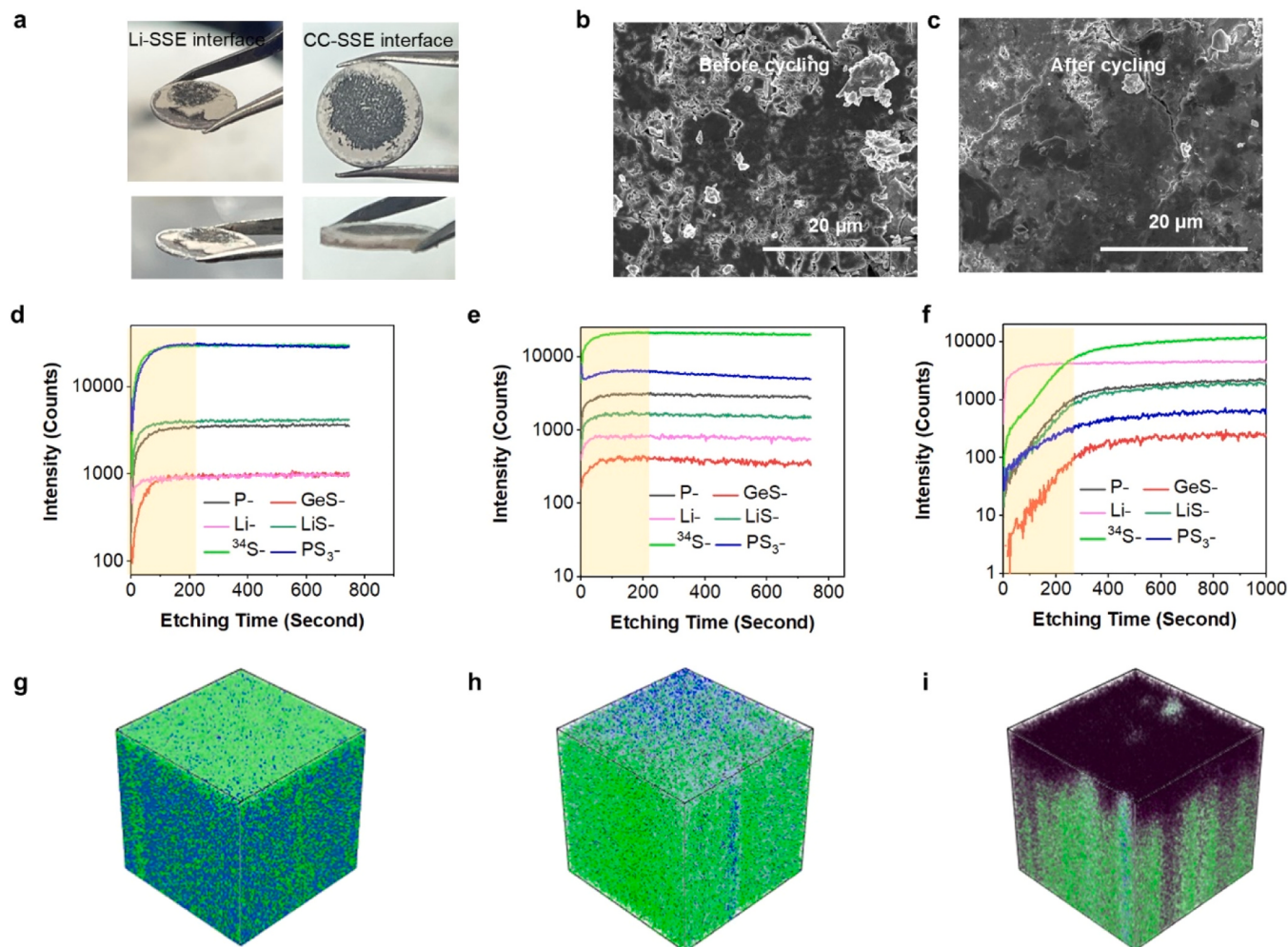


Fig. 5. Characterizations of the interface between Li-SSEs and CC-SSEs. (a) Optical images from top and side view of the surface of Li-LGPS (left) and CC-LGPS (right). (b) and (c) SEM images of the raw surface of LGPS and Steel-LPSC, respectively. (d) ToF-SIMS depth profile of raw surface of LGPS and corresponding 3D reconstruction. (e) ToF-SIMS depth profile of interface of Li-LGPS and corresponding 3D reconstruction. (f) ToF-SIMS depth profile of interface of Steel-LGPS and corresponding 3D reconstruction. (g) - (i) The 3D reconstruction of the depth profiling corresponding to (d) – (f), respectively.

contained SSE (Figure. S8a), while it would be suppressed by the formation of alloy layer as shown in Figure. S8b.

Raman spectra of these three interfaces are also given in Figure. S7. In Figure. S7a, the raw surface shows a peak at 400 cm^{-1} , which can be attributed to the peak of P_2S_6^+ .^[47] However, this peak will shift to 420 cm^{-1} in both Li-LPSC and CC-LPSC surfaces, identifying the formation of PS_4^{3-} . The Raman results reveal that the solid reaction will occur both on the surface and bulk area in LPSC, implying the SEI cannot fully block the electron transfer. The Raman spectra of the LGPS pellet surface also show a significant difference in Figure. S7b. In the raw pellets, the major peaks at 278 cm^{-1} and 420 cm^{-1} represent the PS_4^{3-} and the peaks at 370 cm^{-1} and 384 cm^{-1} represent Li-S and Ge-S, respectively.^[48] The peaks can still be found in the pellet from symmetric cells, though the concentration slightly changes. However, no obvious peak can be found from the pellet in asymmetric cell, since there is no phono dispersion in the Li-Ge alloys. Besides, XPS characterization of the interface between LGPS and Cu also suggested the formation of alloy as shown in Figure. S10. Figure S10a and S10b shows the Ge 3d spectrum before and after cycling, and a small peak around 29 eV occurred after cycling. This peak could be attributed to the Li-Ge alloy peak, manifesting the formation of Li-Ge alloy.^[49] Figure S10c and S10d show the change in S 2d spectrum during, which would suggest the formation of Li_2S in the SEI. Therefore, it can be manifested that the exposure of CC-SEEs could provide sufficient information about SEI. Moreover, an accurate observation of the formation of SEI can be achieved by using coulometric titration time analysis using the Li/SSE/CC configuration.^[50]

Soft breakdown will be aroused from external experimental factors, for example, areal capacity, current density, and cutoff voltage. First, the influence of the physiochemical properties of CC on the electrochemical performance of the asymmetric Li/SSE/CC cells was determined. A comparison between Cu foil and carbon-coated Cu (Cu/C) foil was made as shown in Figure. S11. The cells using carbon-coated Cu foil show comparable performance with steel current collector with a relatively stable RE of around 72 %. The stable RE can be partially attributed to the homogeneous deposition on the small carbon spheres as shown in Figure. S12. Similarly, the Au-coated Cu could also lead to a more homogeneous deposition. The surface morphology of the Au@Cu and LPSC is given in Figure. S13a and S13b, while the morphology after 20 cycles is given in Figure. S13c and S13d. It could be found the Au anode has no apparent change and it was still smooth after cycling, while the LPSC could be denser for a better contact to allow the homogenous deposition. However, for the spare Cu foil, a fast decay of the CE will happen in just 5 cycles and almost no RE after 15 cycles. The SEM and optical images in Figure. S14a and S14b show that side reactions apparently occurred at the interface between the SSE and Cu foil. It was confirmed that the black area was majorly composed of Li_2S by EDAX as shown in Figure. S14c-S14e. Moreover, the results of XPS of the Cu foil after cycling in Figure. S14a identify the formation of CuS. Therefore, the abnormal charge-discharge behavior can be ascribed to the interfacial reaction between Cu and sulfide-based SSEs.^[51] Second, to investigate the influence of porosity and thickness of SSEs, we applied different stacking pressures and amounts of LPSC in the asymmetric cell. As shown in Figure. S15, higher stacking pressure can effectively prolong the cycling time before the soft breakdown due to suppressed porosity. Ideally, the porosity of the SSE layer is less than 5 %.^[52] Moreover, thicker electrolytes could offer better stability resisting the soft breakdown though the lithium reversibility is slightly reduced. Thus, it will be necessary to explore the best condition of SSE thickness and porosity. Constant external stack pressure test is also tested and shown in Figure. S16. When applying a low pressure of 10 MPa, the Li-Cu cells could exhibit a slightly better performance and avoid soft breakdown compared to using module cells without pressure. While the pressure higher than 120 MPa could cause fast short which can be attributed to the lithium penetration and cracks. Third, we assessed the lithium reversibility of Li/LPSC/CC and Li/LGPS/CC asymmetric cells with the capacity of 0.1,

0.2, and 0.5 $\text{mAh}\cdot\text{cm}^{-2}$ at the current density of 0.1, 0.2, and $0.3\text{ mA}/\text{cm}^2$ (Figure. S17a-S17d). It suggests that the “jump point” of lithium reversibility will occur earlier when the areal capacity is higher no matter what kind of SSEs are used. Hence, the areal capacity will majorly influence the occurrence of the soft breakdown. Fourth, in terms of the current density, a fast soft breakdown was exhibited in the Li/LPSC/CC cell at $0.5\text{ mA}\cdot\text{cm}^{-2}$ even at a low area capacity of $0.2\text{ mAh}\cdot\text{cm}^{-2}$. It can be attributed to the current density approaching the critical current density. Last, the influence of cutoff voltage is also evaluated (Figure. S14). It shows that the lithium reversibility almost keeps at the same level in both LPSC and LGPS when lowering the cutoff voltage. Notably, the number of cycles before soft breakdown occurrence shows a different behavior in LPSC and LGPS. In the LPSC, the occurrence of the soft breakdown can be found delayed using the low cutoff voltage at 0.1 V , while no such effects can be found in the LGPS due to the alloy effects of Li-Ge. Considering the practical voltage range in the batteries, the hysteresis effect at low voltage may provide misleading stability.

3. Conclusion

In this work, we assessed the probability of soft breakdown of different solid-state electrolytes (SSEs). Among three sulfide-based SSEs examined, the metal-containing electrolyte (LGPS) demonstrated a greater ability to suppress soft breakdown but inferior RE compared to the non-metal-containing counterparts (LPSC and LPS). The better capability to inhibit soft breakdown and lower RE are attributed to the formation of a Li-Ge interfacial layer between the LGPS and the lithium anode, which effectively consumes lithium dendrites and mitigates their growth. These findings suggest that incorporating metal elements into SSEs could be an effective strategy for inhibiting dendrite formation and preventing soft breakdown. The fundamental insights gained from this study are broadly applicable to the investigation of interfaces between various metal anodes and SSEs and will inform the future design of more stable solid-state electrolytes.

4. Methods

4.1. Cells assembly

$\text{Li}_{10}\text{GeP}_2\text{S}_{12}$ and $\text{Li}_7\text{P}_3\text{S}_{11}$ were supplied by MSE Supplier. $\text{Li}_6\text{PS}_5\text{Cl}$ was supplied from GLABAT Solid-State Battery Inc. To make the solid-state lithium asymmetric cells, 80 mg solid electrolytes were uniaxially pressed into a 10 mm-thick pellet with a diameter of 10 mm under 380 MPa in a homemade model cell (generally the thickness of pellets is around 0.6 mm). Then Li foils were attached on one side of SSE pellets and the current collector could be attached on the other side and then pressed at 50 MPa. The formed Li/SSE/CC cell was then sandwiched between two stainless-steel rods. The symmetric cells were assembled by replacing the current collector with Li foil. The cells were assembled in an ultra-pure argon-filled glove box.

Liquid coin cells were assembled following a previous report.^[29] In sequence, lithium foils, 2 layers of polypropylene separator (Celgard 2400), and counter electrodes (Li or CC) were assembled with the addition of 70 μL of electrolyte. The battery-grade electrolyte used for all experiments was 1 M LiPF_6 in ethylene carbonate (EC): diethyl carbonate (DEC): dimethyl carbonate (DMC) with a 1: 1: 1 vol ratio (as received from Gotion Inc).

4.2. Electrochemistry test

The Li stripping/plating studies were carried out using NEWARE battery analyzers with a voltage range of 0–1.5 V and a current range of $0.1\text{--}3\text{ mA}\cdot\text{cm}^{-2}$ at room temperature. Galvanostatic cycling was employed to evaluate the long cycling stability and the critical current density. The long cycling test is conducted under constant current

densities during repeated one-hour stripping/plating while the potential is recorded over time. In a typical electrochemical test, the cut-off voltage of stripping from Cu was set to 1.5 V.

4.3. Phase characterization

After cycling for 10 cycles at the current density of $0.1 \text{ mA}\cdot\text{cm}^{-2}$ and areal capacity of $0.1 \text{ mAh}\cdot\text{cm}^{-2}$, cycled cells were detached in the argon-filled glovebox, and electrodes were fully removed from electrolytes. The surface of SSE is directly observed after peeling off the electrodes. Scanning electron microscope (SEM) images were obtained by using a Hitachi S-4800 field-emission scanning electron microscope (FE-SEM, acceleration voltage 5 kV). The Raman spectra were collected on a HORIBA Scientific LabRAM Raman spectrometer equipped with a 532 nm laser. ToF-SIMS results were obtained using the IONTOF TOF-SIMS IV at Surface Science Western. During the transfer of the samples from their containers to the instrument, special care was taken to minimize the oxidation of the samples.

The samples were examined using an ION-TOF (GmbH) TOF-SIMS IV equipped with a bismuth cluster liquid metal ion source. A pulsed 25 keV Bi $_3^+$ cluster primary ion beam was used to bombard the sample surface to generate secondary ions from a sample surface. The negative secondary ions were extracted from the sample surface, mass separated, and detected via a reflection-type time-of-flight analyzer, allowing parallel detection of ion fragments having a mass-to-charge ratio up to ~ 900 within each cycle (100 μs). A pulsed, low-energy electron flood was used to neutralize sample charging. Depth profiles of ions were obtained by repeating the cycle of alternatively sputtering the surface in an area of $250 \mu\text{m} \times 250 \mu\text{m}$ with a 3 keV Cs $^+$ beam for 1 s and collecting, upon a waiting time of 0.5 s, ion mass spectra using the Bi $_3^+$ primary ion beam over 128×128 pixels in an area of $128 \mu\text{m} \times 128 \mu\text{m}$ within the sputtered area. The sputtering rate could not be directly measured due to the changing morphology of the samples upon their exposure to air which made the crater depth unmeasurable using a profilometer operated in air. Nevertheless, sputter rates of 0.06 and 0.33 nm/s were estimated on an aluminum film and a gold film (both deposited on a Si wafer), respectively. The sputtering rate for our three samples was likely close to that of the (softer) gold film.

Author contributions

C. Wang and H. Ren conceived the idea. H. Ren conducted all the electrochemical analyses. Z. Yu helped finish the Figure design. X. Lin, J. Fu, J. Luo, Y. Hu, H. Su, W. Li, F. Zhao, Y. Liu, J.T. Kim, and M. Yang participated in some discussions and data collection. H. Ren, Y. Sun, and H. Nie carried out ToF-SIMS experiments. C. Wang and X. Sun supervised the whole project.

CRediT authorship contribution statement

Kim Jung Tae: Data curation. **Zhong Yu:** Visualization. **Yang Mingrui:** Formal analysis. **Lin Xiaoting:** Data curation. **Zhao Feipeng:** Writing – original draft. **Sun Xueliang:** Supervision, Project administration. **Liu Yu:** Data curation. **Ren Haoqi:** Investigation, Formal analysis. **Li Weihan:** Writing – review & editing. **Nie Heng-Yong:** Methodology. **Su Han:** Writing – original draft. **Hu Yang:** Methodology. **Sun Yipeng:** Methodology. **Wang Changhong:** Writing – review & editing, Writing – original draft, Supervision, Conceptualization. **Fu Jiamin:** Validation. **Luo Jing:** Validation.

Declaration of Competing Interest

The authors declare that they have no known competing financial interests or personal relationships that could have appeared to influence the work reported in this paper.

Acknowledgement

This work was supported by the Natural Sciences and Engineering Research Council of Canada (NSERC), Canada Research Chair Program (CRC), Canada Foundation for Innovation (CFI), Ontario Research Fund (ORF), GLABAT Solid-State Battery Inc., and the University of Western Ontario. Prof. C. Wang acknowledges the funding support from the National Natural Science Foundation of China (Grant Nos. W2441017; 22409103), the “Innovation Yongjiang 2035” Key R&D Program (Grant No. 2024Z040; 2025Z063), the Eastern Institute of Technology (EIT), Ningbo.

Supporting information

Evaluation of the asymmetric cells and physical characterization under different conditions including using different kinds of solid electrolytes, varying current density and cutoff volatge.

Appendix A. Supporting information

Supplementary data associated with this article can be found in the online version at doi:[10.1016/j.nanoen.2025.111044](https://doi.org/10.1016/j.nanoen.2025.111044).

Data Availability

Data will be made available on request.

References

- [1] A.M. Bates, Y. Preger, L. Torres-Castro, K.L. Harrison, S.J. Harris, J. Hewson, Are solid-state batteries safer than lithium-ion batteries? Joule 6 (2022) 742–755, <https://doi.org/10.1016/j.joule.2022.02.007>.
- [2] D. Cao, X. Sun, Q. Li, A. Natan, P. Xiang, H. Zhu, Lithium dendrite in all-solid-state batteries: growth mechanisms, suppression strategies, and characterizations, Matter 3 (2020) 57–94, <https://doi.org/10.1016/j.matt.2020.03.015>.
- [3] X.-B. Cheng, R. Zhang, C.-Z. Zhao, F. Wei, J.-G. Zhang, Q. Zhang, A review of solid electrolyte interphases on lithium metal anode, Adv. Sci. 3 (2016) 1500213, <https://doi.org/10.1002/advs.201500213>.
- [4] A.M. Bruck, J. Yin, X. Tong, E.S. Takeuchi, K.J. Takeuchi, L.F. Szczepura, A. C. Marschilok, Reversible electrochemical lithium-ion insertion into the rhenium cluster halogenide-halide $\text{Re}_6\text{Se}_8\text{Cl}_{2x}$, Inorg. Chem. 57 (2018) 4812–4815, <https://doi.org/10.1021/acs.inorgchem.8b00499>.
- [5] E.A. Wu, S. Banerjee, H. Tang, P.M. Richardson, J.-M. Doux, J. Qi, Z. Zhu, A. Grenier, Y. Li, E. Zhao, G. Deysher, E. Sebiti, H. Nguyen, R. Stephens, G. Verbist, K.W. Chapman, R.J. Clément, A. Banerjee, Y.S. Meng, S.P. Ong, A stable cathode-solid electrolyte composite for high-voltage, long-cycle-life solid-state sodium-ion batteries, Nat. Commun. 12 (2021) 1256, <https://doi.org/10.1038/s41467-021-21488-7>.
- [6] Y. Chen, Y. Luo, H. Zhang, C. Qu, H. Zhang, X. Li, The challenge of lithium metal anodes for practical applications, Small Methods 3 (2019) 1800551, <https://doi.org/10.1002/smtd.201800551>.
- [7] T. Asano, A. Sakai, S. Ouchi, M. Sakaida, A. Miyazaki, S. Hasegawa, Solid halide electrolytes with high lithium-ion conductivity for application in 4 V class bulk-type all-solid-state batteries, Adv. Mater. 30 (2018) 1803075, <https://doi.org/10.1002/adma.201803075>.
- [8] X.-B. Cheng, C.-Z. Zhao, Y.-X. Yao, H. Liu, Q. Zhang, Recent advances in energy chemistry between solid-state electrolyte and safe lithium-metal anodes, Chem 5 (2019) 74–96, <https://doi.org/10.1016/j.chempr.2018.12.002>.
- [9] Y.-G. Lee, S. Fujiki, C. Jung, N. Suzuki, N. Yashiro, R. Omoda, D.-S. Ko, T. Shiratsuchi, T. Sugimoto, S. Ryu, J.H. Ku, T. Watanabe, Y. Park, Y. Aihara, D. Im, I.T. Han, High-energy long-cycling all-solid-state lithium metal batteries enabled by silver–carbon composite anodes, Nat. Energy 5 (2020) 299–308, <https://doi.org/10.1038/s41560-020-0575-z>.
- [10] C. Wang, T. Deng, X. Fan, M. Zheng, R. Yu, Q. Lu, H. Duan, H. Huang, C. Wang, X. Sun, Identifying soft breakdown in all-solid-state lithium battery, Joule 6 (2022) 1770–1781, <https://doi.org/10.1016/j.joule.2022.05.020>.
- [11] J. Liang, X. Li, S. Wang, K.R. Adair, W. Li, Y. Zhao, C. Wang, Y. Hu, L. Zhang, S. Zhao, S. Lu, H. Huang, R. Li, Y. Mo, X. Sun, Site-occupation-tuned superionic Li^{+} $\text{ScCl}_3 + x$ halide solid electrolytes for all-solid-state batteries, J. Am. Chem. Soc. 142 (2020) 7012–7022, <https://doi.org/10.1021/jacs.0c00134>.
- [12] J.A. Lewis, S.E. Sandoval, Y. Liu, D.L. Nelson, S.G. Yoon, R. Wang, Y. Zhao, M. Tian, P. Shevchenko, E. Martínez-Paneda, M.T. McDowell, Accelerated short circuiting in anode-free solid-state batteries driven by local lithium depletion, Adv. Energy Mater. 13 (2023) 2204186, <https://doi.org/10.1002/aenm.202204186>.
- [13] T. Dussart, N. Rividi, M. Fialin, G. Toussaint, P. Stevens, C. Laberty-Robert, Critical current density limitation of LLZO solid electrolyte: microstructure vs interface,

- J. Electrochim. Soc. 168 (2021) 120550, <https://doi.org/10.1149/1945-7111/ac44be>.
- [14] X. Li, J. Liang, J. Luo, M. Norouzi Banis, C. Wang, W. Li, S. Deng, C. Yu, F. Zhao, Y. Hu, T.-K. Sham, L. Zhang, S. Zhao, S. Lu, H. Huang, R. Li, K.R. Adair, X. Sun, Air-stable Li₃InCl₆ electrolyte with high voltage compatibility for all-solid-state batteries, Energy Environ. Sci. 12 (2019) 2665–2671, <https://doi.org/10.1039/C9EE02311A>.
- [15] M.J. Counihan, K.S. Chavan, P. Barai, D.J. Powers, Y. Zhang, V. Srinivasan, S. Tepavcevic, The phantom menace of dynamic soft-shorts in solid-state battery research, Joule 8 (2024) 64–90, <https://doi.org/10.1016/j.joule.2023.11.007>.
- [16] D. Cao, K. Zhang, W. Li, Y. Zhang, T. Ji, X. Zhao, E. Cakmak, J. Zhu, Y. Cao, H. Zhu, Nondestructively visualizing and understanding the mechano-electro-chemical origins of “soft short” and “creeping” in all-solid-state batteries, Adv. Funct. Mater. 33 (2023) 2307998, <https://doi.org/10.1002/adfm.202307998>.
- [17] Q. Li, A. Chen, D. Wang, Z. Pei, C. Zhi, Soft shorts[†] hidden in zinc metal anode research, Joule 6 (2022) 273–279, <https://doi.org/10.1016/j.joule.2021.12.009>.
- [18] J. Gu, X. Chen, Z. He, Z. Liang, Y. Lin, J. Shi, Y. Yang, Decoding internal stress-induced micro-short circuit events in sulfide-based all-solid-state li-metal batteries via operando pressure measurements, Adv. Energy Mater. 13 (2023) 2302643, <https://doi.org/10.1002/aenm.202302643>.
- [19] X. Liu, R. Garcia-Mendez, A.R. Lupini, Y. Cheng, Z.D. Hood, F. Han, A. Sharifi, J. C. Idrobo, N.J. Dudney, C. Wang, C. Ma, J. Sakamoto, M. Chi, Local electronic structure variation resulting in li⁺ ‘filament’ formation within solid electrolytes, Nat. Mater. 20 (2021) 1485–1490, <https://doi.org/10.1038/s41563-021-01019-x>.
- [20] F. Han, A.S. Westover, J. Yue, X. Fan, F. Wang, M. Chi, D.N. Leonard, N.J. Dudney, H. Wang, C. Wang, High electronic conductivity as the origin of lithium dendrite formation within solid electrolytes, Nat. Energy 4 (2019) 187–196, <https://doi.org/10.1038/s41560-018-0312-z>.
- [21] Y. Ma, R. Zhang, Y. Tang, Y. Ma, J.H. Teo, T. Diemant, D. Goonetilleke, J. Janek, M. Bianchini, A. Kondrakov, T. Brezesinski, Single- to few-layer nanoparticle cathode coating for thiophosphate-based all-solid-state batteries, ACS Nano 16 (2022) 18682–18694, <https://doi.org/10.1021/acsnano.2c07314>.
- [22] Y. Ma, R. Zhang, Y. Ma, T. Diemant, Y. Tang, S. Payandeh, D. Goonetilleke, D. Kitsche, X. Liu, J. Lin, A. Kondrakov, T. Brezesinski, Interface and electrode microstructure engineering for optimizing performance of the LiNiO₂ cathode in all-solid-state batteries, Chem. Mater. 36 (2024) 2588–2598, <https://doi.org/10.1021/acs.chemmater.4c00301>.
- [23] T. Sun, Z. Li, G. Zhu, L. Wang, D. Ren, T. Shen, L. Lu, Y. Zheng, X. Han, M. Ouyang, Impedance-based online detection of lithium plating for lithium-ion batteries: mechanism and sensitivity analysis, Electrochim. Acta 496 (2024) 144512, <https://doi.org/10.1016/j.electacta.2024.144512>.
- [24] H.J. Choi, D.W. Kang, J.-W. Park, J.-H. Park, Y.-J. Lee, Y.-C. Ha, S.-M. Lee, S. Y. Yoon, B.G. Kim, In situ formed Ag-Li intermetallic layer for stable cycling of all-solid-state lithium batteries, Adv. Sci. 9 (2022) 2103826, <https://doi.org/10.1002/advs.202103826>.
- [25] D. Spencer-Jolly, V. Agarwal, C. Doerrer, B. Hu, S. Zhang, D.L.R. Melvin, H. Gao, X. Gao, P. Adamson, O.V. Magdysyuk, P.S. Grant, R.A. House, P.G. Bruce, Structural changes in the silver-carbon composite anode interlayer of solid-state batteries, Joule 7 (2023) 503–514, <https://doi.org/10.1016/j.joule.2023.02.001>.
- [26] B. Thirumalraj, T.T. Hagos, C.-J. Huang, M.A. Teshager, J.-H. Cheng, W.-N. Su, B.-J. Hwang, Nucleation and growth mechanism of lithium metal electroplating, J. Am. Chem. Soc. 141 (2019) 18612–18623, <https://doi.org/10.1021/jacs.9b10195>.
- [27] W. Deng, X. Yin, W. Bao, X. Zhou, Z. Hu, B. He, B. Qiu, Y.S. Meng, Z. Liu, Quantification of reversible and irreversible lithium in practical lithium-metal batteries, Nat. Energy 7 (2022) 1031–1041, <https://doi.org/10.1038/s41560-022-01120-8>.
- [28] Q. Zhao, Y. Deng, N.W. Utomo, J. Zheng, P. Biswal, J. Yin, L.A. Archer, On the crystallography and reversibility of lithium electrodeposits at ultrahigh capacity, Nat. Commun. 12 (2021) 6034, <https://doi.org/10.1038/s41467-021-26143-9>.
- [29] K.R. Adair, M.N. Banis, Y. Zhao, T. Bond, R. Li, X. Sun, Temperature-dependent chemical and physical microstructure of Li metal anodes revealed through synchrotron-based imaging techniques, Adv. Mater. 32 (2020) 2002550, <https://doi.org/10.1002/adma.202002550>.
- [30] D.H.S. Tan, E.A. Wu, H. Nguyen, Z. Chen, M.A.T. Marple, J.-M. Doux, X. Wang, H. Yang, A. Banerjee, Y.S. Meng, Elucidating reversible electrochemical redox of Li₆PS₅Cl solid electrolyte, ACS Energy Lett. 4 (2019) 2418–2427, <https://doi.org/10.1021/acsenergylett.9b01693>.
- [31] S. Yu, R.D. Schmidt, R. Garcia-Mendez, E. Herbert, N.J. Dudney, J.B. Wolfenstine, J. Sakamoto, D.J. Siegel, Elastic properties of the solid electrolyte Li₇La₃Zr₂O₁₂ (LLZO), Chem. Mater. 28 (2016) 197–206, <https://doi.org/10.1021/acs.chemmater.5b03854>.
- [32] S. Wenzel, S. Randau, T. Leichtweiß, D.A. Weber, J. Sann, W.G. Zeier, J. Janek, Direct observation of the interfacial instability of the fast ionic conductor Li₁₀GeP₂S₁₂ at the lithium metal anode, Chem. Mater. 28 (2016) 2400–2407, <https://doi.org/10.1021/acs.chemmater.6b00610>.
- [33] H. Wan, Z. Wang, S. Liu, B. Zhang, X. He, W. Zhang, C. Wang, Critical interphase overpotential as a lithium dendrite-suppression criterion for all-solid-state lithium battery design, Nat. Energy 8 (2023) 473–481, <https://doi.org/10.1038/s41560-023-01231-w>.
- [34] F. Ding, W. Xu, G.L. Graff, J. Zhang, M.L. Sushko, X. Chen, Y. Shao, M. H. Engelhard, Z. Nie, J. Xiao, X. Liu, P.V. Sushko, J. Liu, J.-G. Zhang, Dendrite-free lithium deposition via self-healing electrostatic shield mechanism, J. Am. Chem. Soc. 135 (2013) 4450–4456, <https://doi.org/10.1021/ja312241y>.
- [35] W. Ping, C. Wang, Z. Lin, E. Hitz, C. Yang, H. Wang, L. Hu, Reversible short-circuit behaviors in garnet-based solid-state batteries, Adv. Energy Mater. 10 (2020) 2000702, <https://doi.org/10.1002/aenm.202000702>.
- [36] S.E. Sandoval, J.A. Lewis, B.S. Vishnugopan, D.L. Nelson, M.M. Schneider, F.J. Q. Cortes, C.M. Matthews, J. Watt, M. Tian, P. Shevchenko, P.P. Mukherjee, M. T. McDowell, Structural and electrochemical evolution of alloy interfacial layers in anode-free solid-state batteries, Joule (2023), <https://doi.org/10.1016/j.joule.2023.07.022>.
- [37] J. Xiao, Q. Li, Y. Bi, M. Cai, B. Dunn, T. Glossmann, J. Liu, T. Osaka, R. Sugiura, B. Wu, J. Yang, J.-G. Zhang, M.S. Whittingham, Understanding and applying coulombic efficiency in lithium metal batteries, Nat. Energy 5 (2020) 561–568, <https://doi.org/10.1038/s41560-020-0648-z>.
- [38] B.D. Adams, J. Zheng, X. Ren, W. Xu, J.-G. Zhang, Accurate determination of coulombic efficiency for lithium metal anodes and lithium metal batteries, Adv. Energy Mater. 8 (2018) 1702097, <https://doi.org/10.1002/aenm.201702097>.
- [39] J.C. Burns, L.J. Krause, D.-B. Le, L.D. Jensen, A.J. Smith, D. Xiong, J.R. Dahn, Introducing symmetric Li-ion cells as a tool to study cell degradation mechanisms, J. Electrochim. Soc. 158 (2011) A1417, <https://doi.org/10.1149/2.084112jes>.
- [40] W. Li, M. Li, H. Ren, J.Tae Kim, R. Li, T.-K. Sham, X. Sun, Nitride solid-state electrolytes for all-solid-state lithium metal batteries, Energy Environ. Sci. (2025), <https://doi.org/10.1038/D4EE04927F>.
- [41] W. Li, M. Li, S. Wang, P.-H. Chien, J. Luo, J. Fu, X. Lin, G. King, R. Feng, J. Wang, J. Zhou, R. Li, J. Liu, Y. Mo, T.-K. Sham, X. Sun, Superionic conducting vacancy-rich Li₃N₃ electrolyte for stable cycling of all-solid-state lithium metal batteries, Nat. Nanotechnol. 20 (2025) 265–275, <https://doi.org/10.1038/s41565-024-01813-z>.
- [42] A.L. Davis, E. Kazヤk, D.W. Liao, K.N. Wood, N.P. Dasgupta, Operando analysis of interphase dynamics in anode-free solid-state batteries with sulfide electrolytes, J. Electrochim. Soc. 168 (2021) 070557, <https://doi.org/10.1149/1945-7111/ac163d>.
- [43] A. Benninghoven, Chemical analysis of inorganic and organic surfaces and thin films by static time-of-flight secondary ion mass spectrometry (TOF-SIMS), Angew. Chem. Int. Ed. Engl. 33 (1994) 1023–1043, <https://doi.org/10.1002/anie.199410231>.
- [44] S. Naderi-Gohar, K.M.H. Huang, Y. Wu, W.M. Lau, H.-Y. Nie, Depth profiling cross-linked poly(methyl methacrylate) films: a time-of-flight secondary ion mass spectrometry approach, Rapid Commun. Mass Spectrom. 31 (2017) 381–388, <https://doi.org/10.1002/rmc.7801>.
- [45] S. Narayanan, U. Ulissi, J.S. Gibson, Y.A. Chart, R.S. Weatherup, M. Pasta, Effect of current density on the solid electrolyte interphase formation at the lithium⁺Li₆PS₅Cl interface, Nat. Commun. 13 (2022) 7237, <https://doi.org/10.1038/s41467-022-34855-9>.
- [46] S.-K. Otto, L.M. Rieger, T. Fuchs, S. Kayser, P. Schweitzer, S. Burkhardt, A. Henss, J. Janek, In situ investigation of lithium metal–solid electrolyte anode interfaces with ToF-SIMS, Adv. Mater. Interfaces 9 (2022) 2102387, <https://doi.org/10.1002/admi.202102387>.
- [47] S. Choi, J. Ann, J. Do, S. Lim, C. Park, D. Shin, Application of rod-like Li₆PS₅Cl directly synthesized by a liquid phase process to sheet-type electrodes for all-solid-state lithium batteries, J. Electrochim. Soc. 166 (2018) A5193, <https://doi.org/10.1149/2.0301903jes>.
- [48] Y. Sun, K. Suzuki, K. Hara, S. Hori, T. Yano, M. Hara, M. Hirayama, R. Kanno, Oxygen substitution effects in Li₁₀GeP₂S₁₂ solid electrolyte, J. Power Sources 324 (2016) 798–803, <https://doi.org/10.1016/j.jpowsour.2016.05.100>.
- [49] M. Wang, Z. Peng, W. Luo, Q. Zhang, Z. Li, Y. Zhu, H. Lin, L. Cai, X. Yao, C. Ouyang, D. Wang, Improving the interfacial stability between lithium and solid-state electrolyte via dipole-structured lithium layer deposited on graphene oxide, Adv. Sci. 7 (2020) 2000237, <https://doi.org/10.1002/advs.202000237>.
- [50] B. Aktekin, L.M. Rieger, S.-K. Otto, T. Fuchs, A. Henss, J. Janek, SEI growth on Lithium metal anodes in solid-state batteries quantified with coulometric titration time analysis, Nat. Commun. 14 (2023) 6946, <https://doi.org/10.1038/s41467-023-42512-y>.
- [51] M. Li, B. Wang, J. Ma, Z. Wang, Y. Liang, Z. Wang, L. Zhang, Y. Tang, Q. Huang, J. Huang, Understanding the stability of copper current collector with sulfide electrolyte in all-solid-state batteries, Adv. Energy Mater. 14 (2024) 2303156, <https://doi.org/10.1002/aenm.202303156>.
- [52] M.S. Diallo, T. Shi, Y. Zhang, X. Peng, I. Shozib, Y. Wang, L.J. Miara, M.C. Scott, Q. H. Tu, G. Ceder, Effect of solid-electrolyte pellet density on failure of solid-state batteries, Nat. Commun. 15 (2024) 858, <https://doi.org/10.1038/s41467-024-45030-7>.